Journal of Zhejiang University-SCIENCE A
www.jzus.zju.edu.cn; www.springer.com/journal/11582
E-mail: jzus_a@zju.edu.cn

Research Article
https://doi.org/10.1631/jzus.A2600050

Weak fault feature diagnosis method for electric drive systems based on a multisource feature fusion selection mechanism

Cong YUE✉, Jingwen KANG, Yonghao ZHAO, Ping CHENG

Logistics Engineering College, Shanghai Maritime University, Shanghai 201306, China

Abstract: Electric drive systems (EDS) feature high integration and strong nonlinearity, which renders weak fault identification a challenging task. Acoustic particle velocity signals employed for noncontact fault monitoring are prone to contamination by noise and redundant features. This contamination seriously interferes with weak fault extraction and reduces diagnostic stability. To overcome the limitations of conventional single or multiple feature selection strategies, this paper proposes an information entropy-based multisource feature fusion selection (IE-MSFS) method. The proposed method can effectively eliminate redundant information and enhance the characterization ability of weak fault features. Based on the EDS acoustic particle velocity signals collected in the laboratory, a comparative analysis with vibration signals is carried out on three typical weak fault types through machine-learning evaluation. The results verify that the proposed fault diagnosis method scheme exhibits outstanding and stable weak fault recognition performance, with a diagnostic accuracy exceeding 95.2%. Further tests demonstrate that the established scheme has favorable robustness and generalization ability for EDS weak fault diagnosis.

Key words: Particle velocity signal; Weak fault diagnosis; Multisource feature fusion selection; Enhanced feature extraction

1 Introduction

Electric drive systems (EDS), as a pivotal mechanical component, play an indispensable role in critical fields, including aerospace and shipping, serving as the core power support for high precision and high reliability. With the rapid advancement of industrial development, increasingly stringent requirements are imposed on the reliability of EDS (Husain et al., 2021). Rolling bearings operate continuously under high-speed and complex loading conditions. Early-stage faults often manifest as faint and low-amplitude disturbances (Nawfal Mustafa, 2021), readily obscured by ambient noise and other interferences to greatly hinder fault classification and identification. Consequently, in-depth investigation of these subtle faults is pivotal to achieving accurate fault diagnosis.

Fault diagnosis techniques based on vibration signals have reached a relatively mature stage. Its core procedures include signal acquisition by sensors, denoising preprocessing, fault feature extraction, and fault classification and identification via machine learning (ML) algorithms. However, the application of such methods in EDS is constrained. On the one hand, EDS possesses complex internal structures. On the other hand, vibration sensors need to be closely attached to equipment surfaces, leading to inconvenient installation and potential safety hazards (Kuntoğlu et al., 2021). To address these limitations, Yao et al. (2025) adopted noncontact acoustic signals, which can effectively capture fault information owing to their high sensitivity to fault characteristics. To further strengthen weak fault signatures in acoustic signals, Hou et al. (2022) proposed a sparsity-oriented adjusted multipoint optimal minimum entropy deconvolution method. On this basis, Liu et al. (2025) developed a convolutional neural network (CNN)–temporal convolutional network (TCN) model, which achieves reliable fault feature detection from acoustic signals under complex noise interference.

The aforementioned research effectively extracts bearing fault characteristics from acoustic signals. Nevertheless, these methods are still vulnerable to

✉ Cong YUE, yuecong234@163.com
Cong YUE, https://orcid.org/0000-0002-2532-7195

Received Jan. 23, 2026; Revision accepted May 25, 2026;
Crosschecked July 10, 2026

© Zhejiang University Press 2026

environmental noise, and traditional denoising strategies often fail to achieve satisfactory performance. This limitation is particularly prominent under the superposition of multiple noise sources (Yang et al., 2019). Conventional filtering struggles to effectively separate these signals, posing challenges for subsequent feature extraction and identification (Long et al., 2021). Mitigating the impact of this issue, Meng et al. (2022) employed the kurtosis criterion to apply intrinsic mode function (IMF) filtering, which bridges the connection between the actual fault spectrum and theoretical fault characteristic frequencies. To improve the extraction accuracy of complex signaling components, Miao et al. (2023) designed an adaptive finite impulse response filter for decomposing different modes and utilized correlated kurtosis to extract mechanical fault features. Targeting residual noise interference in complex working conditions, Chen BY et al. (2021) proposed an adaptive time-varying morphological filtering method. This method eliminates irrelevant interference components with the aid of diagonal slice spectrum analysis.

As the complexity of acoustic signals increases, directly extracting a large number of features tends to introduce noise and redundant data, thereby reducing the accuracy and stability of diagnostic models. In the study of complex dynamic systems, issues related to stability, uncertainty, and anti-interference performance have long been important topics (Manivannan et al., 2020). For this reason, reasonable feature selection and robust indicator evaluation have become essential steps to improve fault diagnosis performance. To address redundant feature interference, Lao et al. (2023) introduced an adaptive feature selection method to reduce redundant features, thereby enhancing the ability to distinguish similar feature samples within multi-classification models. Extending this adaptive strategy, Wang et al. (2021) established a multi-criteria mathematical model. It efficiently extracts diverse low-dimensional near-optimal fault feature subsets. Aiming to address the inherent limitation of single evaluation metrics, Wang et al. (2022) devised a weighted fusion indicator based on kurtosis and spectral negative entropy. This design overcomes the drawbacks of single indicators and follows the systematic analysis principles for complex systems (Jusup et al., 2022).

Traditional diagnostic methods are limited by poor adaptability, insufficient noise resistance, and low diagnostic accuracy (Raj et al., 2025; Zhao et al., 2025). ML models can effectively overcome these limitations through their robust feature learning and pattern recognition capabilities, enabling precise fault identification and classification. Wang et al. (2024) constructed a feature matrix that characterizes fault modes and severity through recurrence quantization analysis, employing Bayesian optimization to determine the optimal parameters for the support vector machine (SVM). Experiments confirm that the method is capable of effectively distinguishing fault modes and quantifying fault severity levels. Wan et al. (2021) developed an efficient rolling element bearing fault diagnosis method based on Spark and an improved random forest algorithm by eliminating the decision trees with low classification accuracy and prone to repeated voting from the original random forest. Targeting reliable feature extraction, Tang et al. (2024) proposed a trustworthy multiscale secondary attention-embedded CNN for bearing fault diagnosis, introducing a reliable multiscale learning strategy to achieve dependable fault identification.

Current research focuses on screening high-dimensional feature sets following feature extraction, employing dimension reduction methods, such as principal component analysis (PCA) (Odhiambo Omuya et al., 2021) or linear discriminant analysis (LDA) (Lu et al., 2025), to select effective features. Current methods can reduce feature dimensionality to a certain extent. However, these methods still have obvious limitations. Signal reconstruction inevitably mixes noise components with fault-related features. This process preserves many invalid features and increases the difficulty of subsequent feature extraction and fault identification. In practical applications, multiple signal processing procedures are needed, including signal decomposition, reconstruction, and feature screening. Repeated processing operations may cause the loss of subtle fault information and further reduce diagnostic accuracy. Acoustic signals are highly susceptible to strong background noise, which easily masks weak fault characteristics. Affected by redundant feature interference, existing methods struggle to maintain stable robustness under such complex working conditions.

Challenges faced by existing methods. The present study proposes a feature selection method, namely, the information entropy-based multisource feature fusion selection (IE-MSFS), which analyses IMFs to

extract latent fault characteristics at different frequency scales. In this paper, we propose a novel hybrid fault diagnosis model, designated as CIR-PS. Initially, raw vibration signals are decomposed using complete ensemble empirical mode decomposition with adaptive noise (CEEMDAN). Subsequently, composite multiscale reverse weighted permutation entropy (CMRWPE) is extracted from the resultant IMFs to characterize their nonlinear dynamics. To mitigate dimensionality issues, IE-MSFS is then applied to refine the feature subset. Finally, SVM classifier, with its hyperparameters fine-tuned via particle swarm optimization (PSO), is employed for accurate fault identification.

2 Theoretical methods

This section focuses on the development of CIR-PS, beginning with an exposition of the core principles and implementation steps of IE-MSFS. The theoretical framework of CMRWPE is subsequently outlined, culminating in a detailed description of the workflow for the proposed model.

2.1 IE-MSFS framework

The IE-MSFS uses CEEMDAN (Chen WG et al., 2021) for original signal decomposition. This effectively mitigates environmental noise interference. The interference targets the extraction of subtle fault features from signals. The final decomposition result and residual signals of CEEMDAN are defined as follows:

$$\begin{cases} v(t)=\sum_{m=1}^{M} i_m(t)+r_M(t), \\ r_M(t)=v(t)-\sum_{m=1}^{M} i_m(t), \end{cases} \tag{1}$$

where $v(t)$ denotes the original data sequence of the signal; t denotes the discrete sampling time point; M denotes the total number of IMF components obtained from the decomposition; $i_m(t)$ denotes to the mth IMF obtained by decomposition; $r_M(t)$ denotes the residual component after decomposition.

IE-MSFS identifies IMF components containing meaningful information and employs information entropy to select optimal time-domain features, thereby overcoming the limitation of traditional feature selection methods that focus solely on the features themselves. It further incorporates the Pearson correlation coefficient (Gong et al., 2024) for evaluation. This approach quantifies the association between each component and the original signal.

The specific steps of IE-MSFS are as follows:

Step 1: the original data sequence is denoted as $v(t)$. CEEMDAN decomposes the original signal into IMF sequences s, with the kth IMF component is denoted as $\boldsymbol{I}_k$ (k=1, 2, ⋯, 8).

Step 2: for each IMF, six typical time-domain metrics $\boldsymbol{T}_{k,t}$ are calculated: mean, variance, standard deviation, kurtosis, skewness, and root mean square. These are sorted in this sequence, yielding a total matrix $\boldsymbol{T}_{k,t}$ of size 6×k. The formula for $\boldsymbol{T}_{k,t}$ is defined as:

$$\boldsymbol{T}_{k,t}=\begin{cases} \frac{1}{N}\sum_{j=1}^{N} i_{k,j}, \\ \frac{1}{N-1}\sum_{j=1}^{N}(i_{k,j}-\boldsymbol{T}_{k,1})^2, \\ \sqrt{\boldsymbol{T}_{k,2}}, \\ \frac{1}{N}\sum_{j=1}^{N}\left(\frac{i_{k,j}-\boldsymbol{T}_{k,1}}{\boldsymbol{T}_{k,3}}\right)^4-3, \\ \frac{1}{N}\sum_{j=1}^{N}\left(\frac{i_{k,j}-\boldsymbol{T}_{k,1}}{\boldsymbol{T}_{k,3}}\right)^3, \\ \sqrt{\frac{1}{N}\sum_{j=1}^{N} i_{k,j}^2}, \end{cases} \qquad (t=1, 2, \cdots, 6), \tag{2}$$

where N denotes the total number of sampling points of single IMF sequence; $i_{k,j}$ denotes the jth sampling value of the kth IMF component; $\boldsymbol{T}_{k,1}$–$\boldsymbol{T}_{k,6}$ denote the six time-domain feature metrics calculated from the kth IMF.

Step 3: information entropy $E(H, \boldsymbol{T}_{k,t})$ is utilized to evaluate the discrepancy between time-domain metrics and raw data, defined as follows:

$$E(H, \boldsymbol{T}_{k,t})=\left| H(\boldsymbol{Y})+\sum_{k=1}^{8} p(\boldsymbol{T}_{k,t})\lg p(\boldsymbol{T}_{k,t}) \right|, \tag{3}$$

where $H(\boldsymbol{Y})$ is the entropy of the original data information; $\boldsymbol{Y}$ denotes the original acoustic signal sequence; $p(\boldsymbol{T}_{k,t})$ denotes the probability distribution of the acquired data.

Step 4: calculate the Pearson correlation coefficient ρ_k between $\boldsymbol{I}_k$ and the original data. Assuming $\boldsymbol{I}_k=[i_{s_k}, i_{s_{k+1}}, \cdots, i_{e_k}]$, where s_k and e_k are the start and

end indices of the IMF interval, respectively, and i_{s_k} and i_{e_k} are the IMF sampling values corresponding to s_k and e_k, respectively; the formula for calculating the absolute value of ρ_k for the original data and the kth IMF is as follows:

$$\rho_k=\left|\frac{\sum_{j=s_k}^{e_k}(y_j-\overline{\boldsymbol{Y}})(i_{k,j}-\overline{\boldsymbol{I}}_k)}{\sqrt{\sum_{j=1}^{N}(y_j-\overline{\boldsymbol{Y}})^2}\sqrt{\sum_{j=s_k}^{e_k}(i_{k,j}-\overline{\boldsymbol{I}}_k)^2}}\right|, \tag{4}$$

$$\overline{\boldsymbol{I}}_k=\frac{1}{e_k-s_k+1}\sum_{j=s_k}^{e_k}i_{k,j}, \tag{5}$$

where y_j denotes the jth sampling point of the original signal; $\overline{\boldsymbol{Y}}$ denotes the global mean of the original signal; $\overline{\boldsymbol{I}}_k$ denotes the mean value of the kth IMF within the selected interval.

Step 5: IMF selection is performed based on the time-domain features and correlation coefficients obtained from steps 3 and 4. Fig. 1 illustrates the basic schematic of the IE-MSFS method.

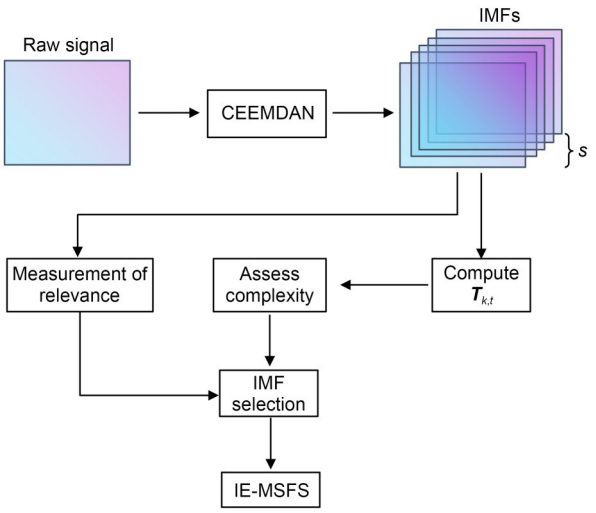


Fig. 1 Multisource joint feature selection mechanism based on IE-MSFS

Fig. 1 illustrates the proposed IE-MSFS. The raw signal is decomposed into intrinsic mode functions by CEEMDAN. Each IMF is evaluated in two dimensions, including relevance to the original signal and complexity, based on the computed entropy indicators. Optimal IMFs are selected to suppress noise and redundant components and form the feature set. This process aims to extract discriminative weak fault features and eliminate interference to improve the reliability of subsequent fault diagnosis.

2.2 Composite multiscale reverse weighted permutation entropy

Reverse weighted permutation entropy (RWPE) (Gao et al., 2023) constitutes an enhanced algorithm derived from permutation entropy (PE). PE exhibits strong robustness to noise but fails to account for amplitude variations between reconstruction sequences, resulting in shortcomings in impact amplitude analysis. RWPE addresses this deficiency by employing amplitude weighting and reverse weighting strategies, enabling the extraction of fault characteristics from complex raw data. The calculation formula for RWPE E_{w} is as follows:

$$E_{\mathrm{w}}(\boldsymbol{X}^{(q,t)})=\sum_{r=1}^{q!}\left(P(\pi_r)-\frac{1}{q!}\right)^2, \tag{6}$$

where $\boldsymbol{X}^{(q,t)}$ denotes the tth time-domain feature set of the qth IMF component, and q is the embedding dimension; $P(\pi_r)$ denotes the probability of the rth permutation pattern π_r.

Composite multiscale coarsening (CMSC) analysis overcomes the issue of neglecting subtle fault information inherent in multiscale coarsening (MSC) based on nonrepeating neighboring mean entropy calculations. This method precisely captures detailed temporal variations in signals, significantly enhancing the identification capability of fault characteristic information in nonlinear and nonstationary signals. The specific formula for CMSC is as follows:

$$Y_{a,b}^{S}=\frac{1}{a}\sum_{i=(j-1)a+b}^{ja+b-1}y_i,\ (a=1,\ 2,\ \cdots,\ S;\ b=1,\ 2,\ \cdots,\ a), \tag{7}$$

where $Y_{a,b}^{S}$ denotes the coarse-grained segment mean at scale a; a and b denote the coarse-grained scale and segment offset, respectively; S denotes the maximum scale of coarse-grained processing; y_i denotes the time series.

Fig. 2 shows the core differences between traditional MSC and CMSC. The top row represents the original signal sequence, while the bottom rows depict

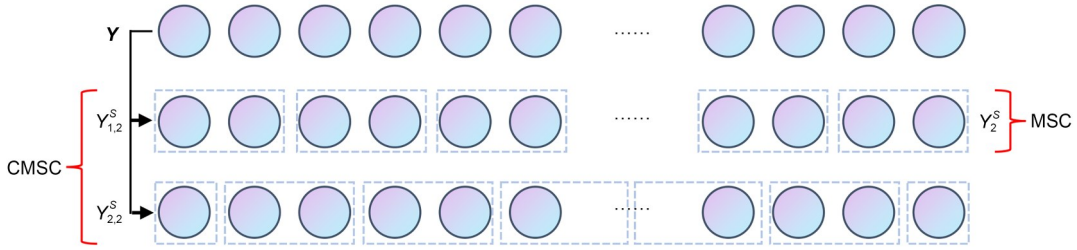


Fig. 2 Comparison of principles between MSC and CMSC. Y_2^S denotes the coarse-grained sequence of MSC with scale a=2

the CMSC coarsening processes under different parameter settings. By introducing multiple window division patterns, CMSC effectively addresses the drawbacks of information loss and scale dependence in traditional MSC, generating more complete multiscale signal representations and providing a more stable and reliable data foundation for subsequent entropy analysis.

CMRWPE is constructed by combining CMSC with RWPE. By incorporating parallel subsequence calculations to compute average entropy values, it can fully extract hidden features within signals. The CMRWPE set calculation formula is defined below:

$$\boldsymbol{C}=\left\{E_{\mathrm{c}}(\boldsymbol{X}_{a,b}^{(q,i)}),\ i=1,\ 2,\ \cdots,\ S\right\}, \tag{8}$$

where $\boldsymbol{C}$ is used to store all feature results from multiscale entropy analysis; $E_{\mathrm{c}}(\boldsymbol{X}_{a,b}^{(q,i)})$ denotes the CMRWPE value of coarse-grained sequence $\boldsymbol{X}_{a,b}^{(q,i)}$; $\boldsymbol{X}_{a,b}^{(q,i)}$ denotes the ith coarse-grained feature set under embedding dimension q.

2.3 Fault diagnosis framework CIR-PS

The flowchart of the proposed CIR-PS framework for the diagnosis of subtle faults in EDS bearings is shown in Fig. 3. This diagram illustrates the whole process ranging from signal collection to fault classification and elaborates the cooperation of all functional modules.

The study employs the PSO-SVM (Zhang et al., 2020). PSO efficiently searches for the optimal parameters of SVM. It enhances the model's capability to process complex data and reduces noise interference.

The specific steps of the CIR-PS fault diagnosis model are as follows:

(1) Acoustic signals were collected via sensors;

(2) The captured acoustic signals are decomposed using the CEEMDAN method to obtain multiple IMFs, thereby reducing noise interference;

(3) Employ IE-MSFS for filtering and retaining IMFs containing effective feature information to enhance fault feature extraction capability;

(4) Calculate feature entropy values for the filtered IMFs using CMRWPE to uncover subtle fault characteristics;

(5) Utilize PSO-SVM to identify subtle faults in the EDS based on the obtained feature entropy values.

3 Experimental study

The validity and stability of the proposed method were verified through bench testing conducted in our EDS testing laboratory (Yue et al., 2024). The EDS, as depicted in Fig. 4, constitutes a critical component of the test system. It serves as the core data acquisition unit responsible for collecting raw signals under different working conditions for subsequent fault diagnosis analysis. All tests strictly adhered to standardized operating conditions, with a constant rotational speed of 1000 r/min and a constant torque of 50 Nm. Each single condition measurement lasted no less than 120 s and was paired with a 20 kHz sampling frequency to ensure sufficient cyclic samples. A particle velocity sensor (PVS) was mounted on a customized bracket external to the EDS to capture the acoustic particle velocity signal (APVS). This signal can directly quantify vibration states, offering advantages in identifying weak fault information. Integrated electronics piezo electric (IEPE) and micro-electro mechanical system (MEMS) sensors were employed to acquire dynamic signals, with key sensor parameters referenced from Yue et al. (2025).

Rolling bearings of model NSK-6307 were employed to design faults, considering four health states: rolling element fault (REF), outer ring fault (ORF), inner ring fault (IRF), and normal state (NOR). This study employs artificially designed micro faults (both

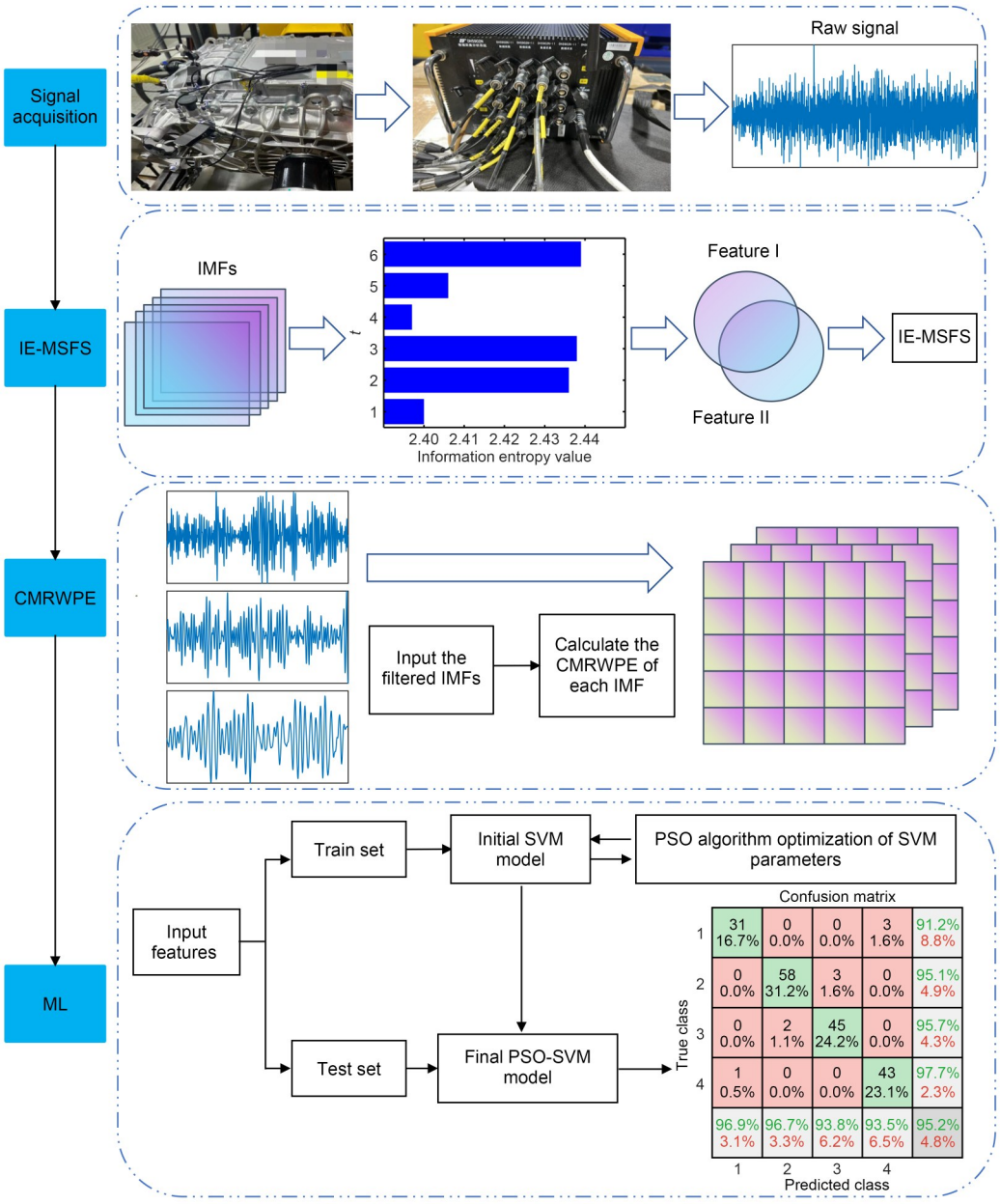


Fig. 3 Process flow of the CIR-PS fault diagnosis model

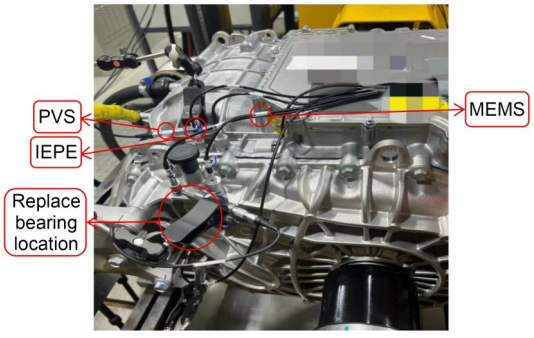


Fig. 4 EDS experimental bench

the fault depth and width are relatively small) to simulate the characteristic patterns of early-stage and subtle faults in equipment. Detailed information regarding the bearing fault design is presented in Table 1.

Fig. 5 presents time-domain waveforms and frequency spectra of APVS, and Fig. 6 shows the time-domain curves of vibration signals collected by IEPE and MEMS sensors. The acoustic signal exhibits chaotic and irregular fluctuations in the time domain, while its fault-related spectral components are widely distributed and scattered across the frequency axis. Its fault-related

frequency components are widely dispersed. These features mask valid fault information and obscure characteristic fault frequencies, thus hindering direct fault diagnosis based on original signals.

To further analyze the fault signal and identify its intrinsic components, the CEEMDAN method was employed to decompose an REF signal. The spectra of the resulting IMFs are shown in Fig. 7. This step aims to isolate the frequency components associated with the fault from those dominated by noise or driven by trends, thereby enabling an analysis of how different IMFs carry distinct fault information.

After CEEMDAN, as shown in Fig. 7, diverse IMF components are acquired with distinct spectral characteristics. High-order components from IMF 6 to IMF 10 are mainly distributed below 500 Hz and gather energy near the direct current, which reflects low-frequency trends and background noise. By comparison, low-order components from IMF 1 to IMF 5 cover the frequency range of 0 to 4000 Hz and contain major bearing fault frequency bands. Among them, IMF 1 to IMF 3 carry sufficient medium- and high-frequency information, and IMF 4 to IMF 5 concentrate energy in medium- and low-frequency bands, matching the theoretical fault characteristic frequencies well. The above results prove that the selected IMFs can fully extract valid fault information and verify the rationality of the screening strategy based on kurtosis and the correlation coefficient.

Table 1 Settings of different rolling bearing faults

Fault type	Fault width (mm)	Fault depth (mm)	Category
REF	≈3.0	≈1.0	1
ORF	≈0.6	≈1.0	2
IRF	≈0.6	≈1.0	3
NOR	No defects	No defects	4

4 Comparative analysis

The APVS serves as the research target, and the IE-MSFS parameters were determined. Signal-to-noise ratio (SNR) tests and ablation experiments verified the feature extraction stability and CIR-PS module contributions. A model accuracy comparison was conducted to characterize the fault detection ability of various algorithms under different signal quality scenarios.

4.1 IE-MSFS parameter analysis

Random sampling of the weak fault APVS was conducted, followed by IE-MSFS analysis. CEEMDAN

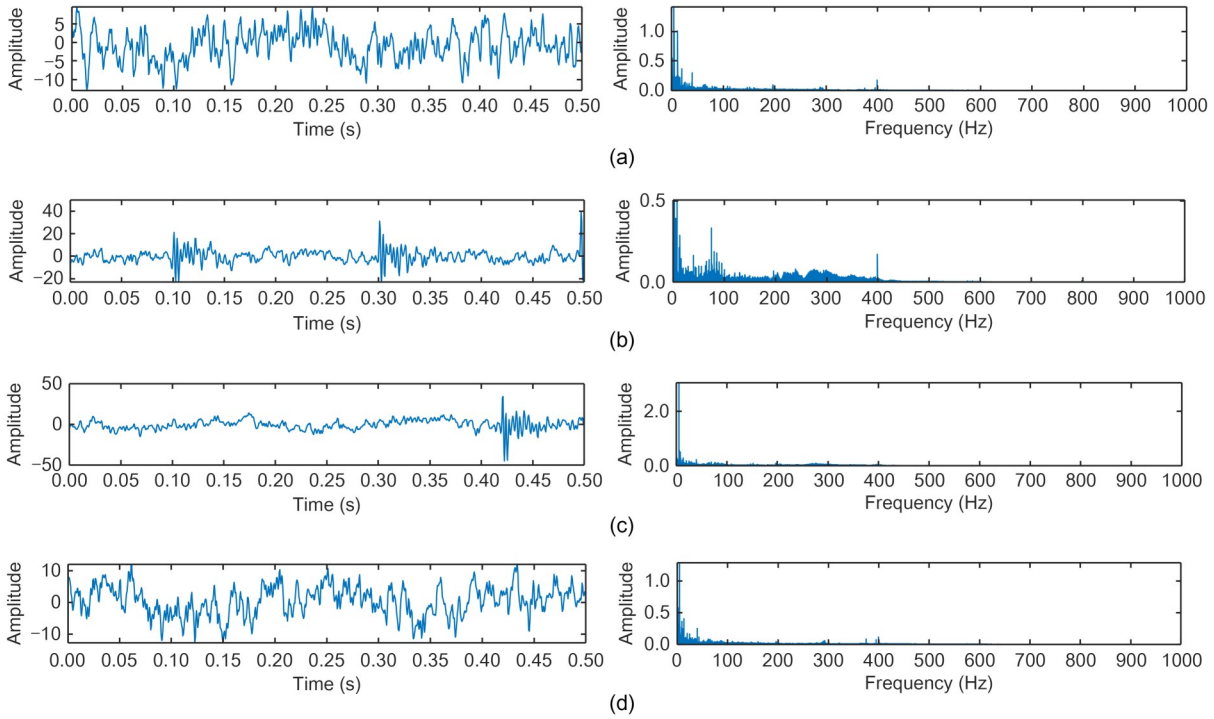


Fig. 5 Time-domain plots and frequency spectra of the APVS: (a) REF; (b) ORF; (c) IRF; (d) NOR

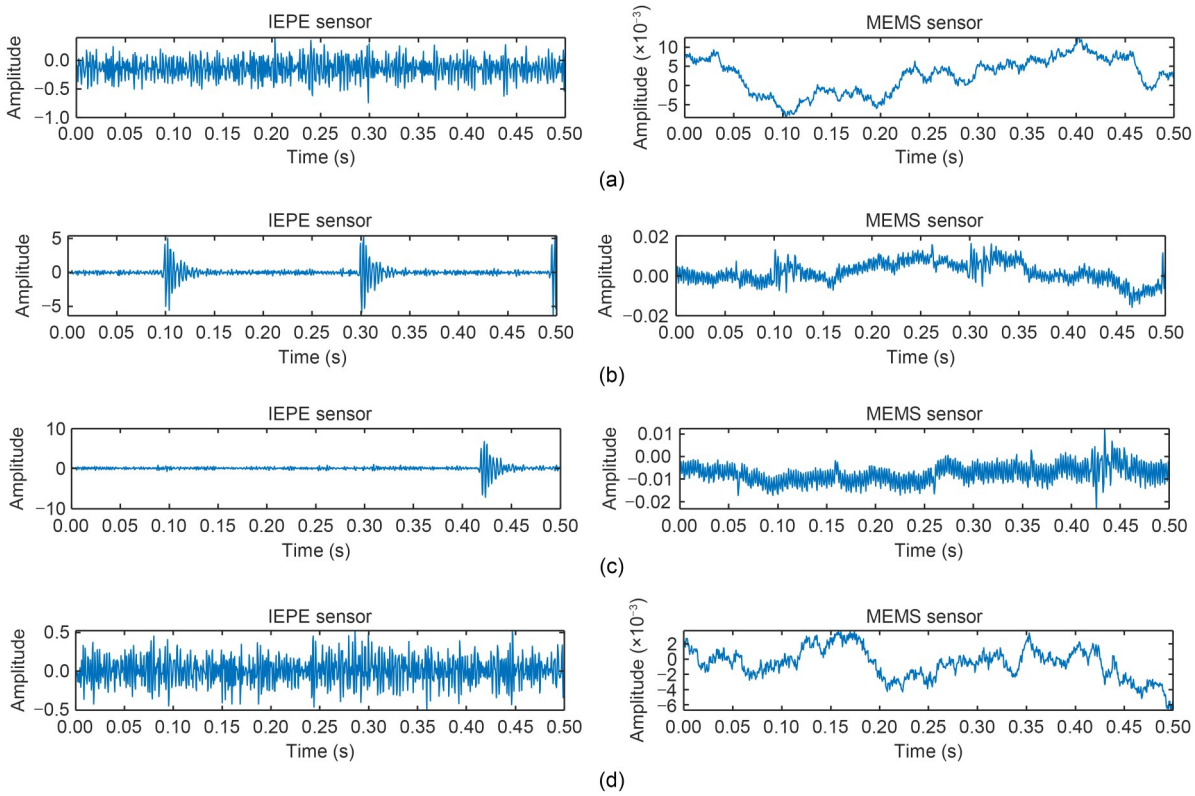


Fig. 6 Time-domain plots of vibration signals from IEPE and MEMS sensors: (a) REF; (b) ORF; (c) IRF; (d) NOR

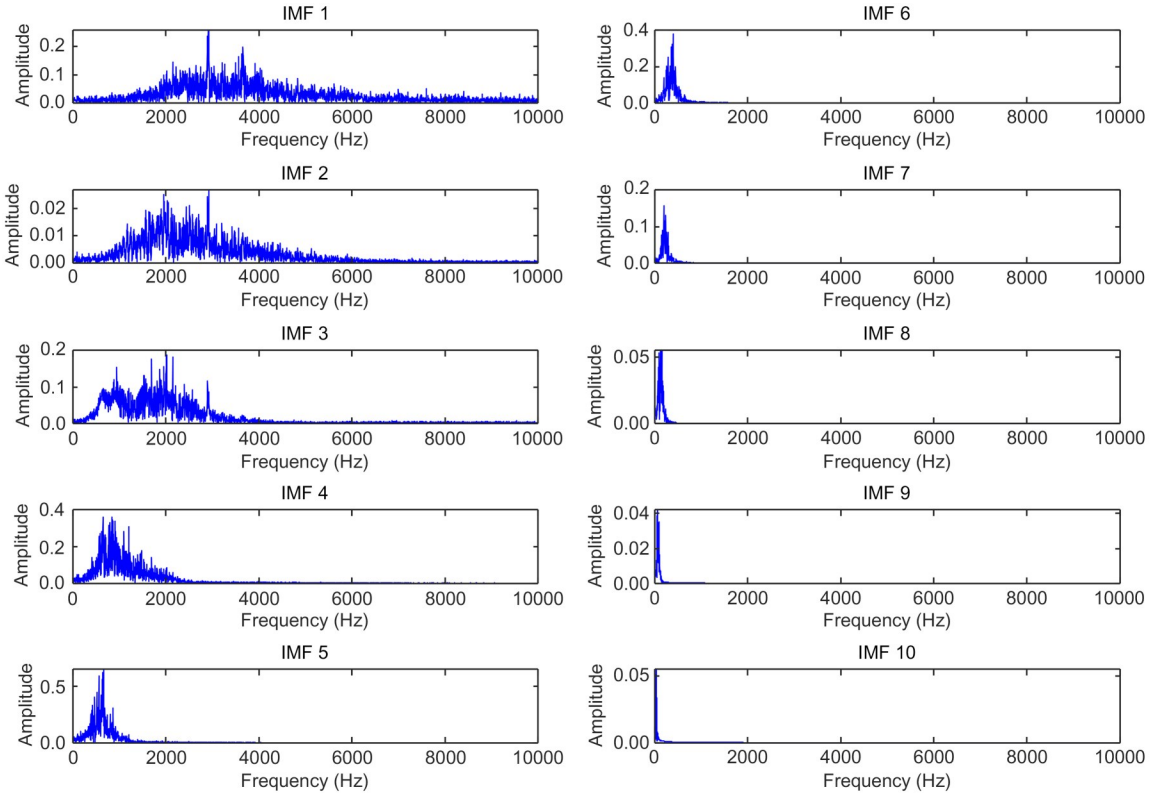


Fig. 7 IMF spectrograms based on the CEEMDAN method

decomposition yielded 12 IMF components. A matrix of size 12×6 was constructed based on $\boldsymbol{T}_{k,t}$, integrating information entropy quantification features with indicator importance.

Fig. 8 shows the information entropy values of six different time-domain features calculated by the proposed method, revealing that the information entropy value is minimal at t=4 (as indicated by the red dashed box), with the corresponding kurtosis more effectively reflecting fault characteristics. As kurtosis is constrained by time-domain analysis, the Pearson correlation coefficient is introduced to assist in screening.

Fig. 9 quantifies the stability of IMFs through the distribution of kurtosis and correlation coefficients. In Fig. 9a, outliers in IMF 2 indicate intermittent impacts and persistent wear. In Fig. 9b, high-frequency components (IMF 1–IMF 7) contain fault information, especially IMF 4. Based on these results, IMF 3 is selected to ensure the reliability of subsequent analysis.

The preliminary IMF parameter n is set to 3, where n denotes the IMF order. The diagnostic accuracy of weak faults is analyzed under different values of n. All experiments were repeated five times to minimize random variation. The maximum, minimum, and mean accuracy are presented in Table 2. The overall average accuracy and processing time are further summarized in Table 3.

Table 2 indicates that the average diagnostic accuracy for ORF and IRF (categories 2 and 3) across all parameter types reached approximately 96.0%. Only when n=3 did the diagnostic performance for

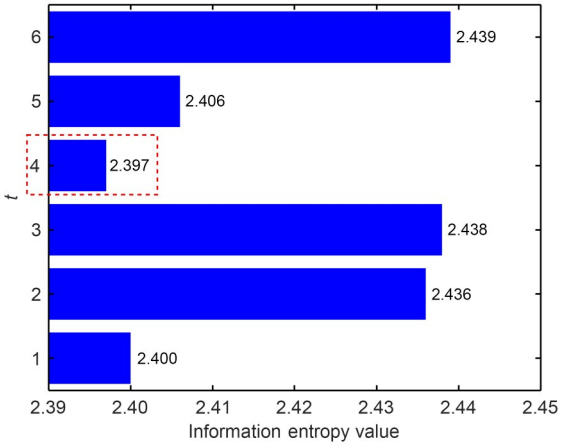


Fig. 8 Horizontal bar chart of the information entropy values of six different time-domain features

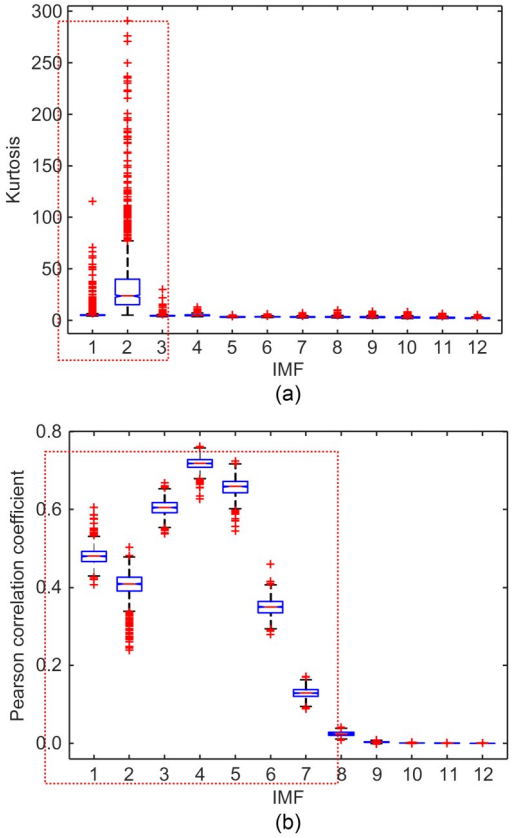


Fig. 9 Box diagrams of APVS: (a) kurtosis; (b) Pearson correlation coefficient

Table 2 Fault diagnosis accuracy under different n values

n	REF (%)			ORF (%)			IRF (%)			NOR (%)		
	Max	Min	Mean	Max	Min	Mean	Max	Min	Mean	Max	Min	Mean
1	95.1	80.2	88.5	97.1	74.8	90.4	99.5	97.6	98.8	100.0	95.3	97.6
2	94.1	90.1	92.3	96.4	93.8	95.4	98.0	95.9	96.6	96.0	90.3	93.1
3	95.7	92.2	94.6	99.7	92.7	96.1	100.0	93.2	96.3	100.0	96.1	98.0
4	92.6	84.9	89.9	96.2	95.1	95.6	99.2	94.5	97.6	97.2	93.8	94.9
5	91.3	82.6	87.5	98.3	90.2	95.2	99.2	95.0	97.9	95.9	82.7	88.6
6	92.2	82.9	86.9	99.2	95.2	96.5	99.1	95.3	97.1	93.0	89.7	92.4
7	86.5	81.2	84.6	98.4	96.7	97.5	99.2	96.6	97.5	91.7	86.8	88.5
8	87.0	80.0	84.5	99.1	96.2	97.3	99.2	97.4	98.3	90.2	80.5	84.5

Table 3 Mean accuracy and average processing time under different *n* values

n	Mean accuracy (%)	Average processing time (s)
1	93.10	27.9
2	93.40	29.6
3	95.70	30.2
4	94.20	38.8
5	92.50	42.1
6	92.40	43.6
7	91.90	43.5
8	90.10	43.9

REF versus NOR (categories 1 and 4) demonstrate superiority.

Table 3 shows that with the increment of the parameter *n*, the diagnostic accuracy initially rises before declining, while the average processing time progressively increases. When *n*=3, the utilization of effective feature information reaches an optimum, achieving a peak diagnostic accuracy of 95.7%. Beyond *n*=3, the introduction of redundant feature information interferes with the extraction of effective features, ultimately leading to a decline in performance. Balancing accuracy and computational cost, *n*=3 is determined as the optimal parameter. The proposed CIR-PS model screens effective IMFs to suppress interference caused by redundant features. This approach significantly enhances the representation capability of weak fault features.

4.2 Signal-to-noise ratio experimental analysis

To validate the performance of IE-MSFS in improving the feature extraction stability of acoustic signals, the entropy values from the CIR (IE-MSFS coupled with CMRWPE) and CMRWPE methods are compared at multiple scales. Comparative analysis is conducted under SNR levels of 5, 10, 15, and 20 dB, where different noise environments are constructed by injecting Gaussian white noise into the original signal.

To verify the noise robustness of the proposed feature extraction method, the comparison results of CMRWPE and CIR under different SNR levels are presented in Fig. 10.

As shown in Fig. 10, there is a significant disparity in the entropy values obtained by the two methods. The CMRWPE curves exhibit relatively stable variation across scales, whereas the CIR curves show a gradual decline with clear divergence at low scales. Between

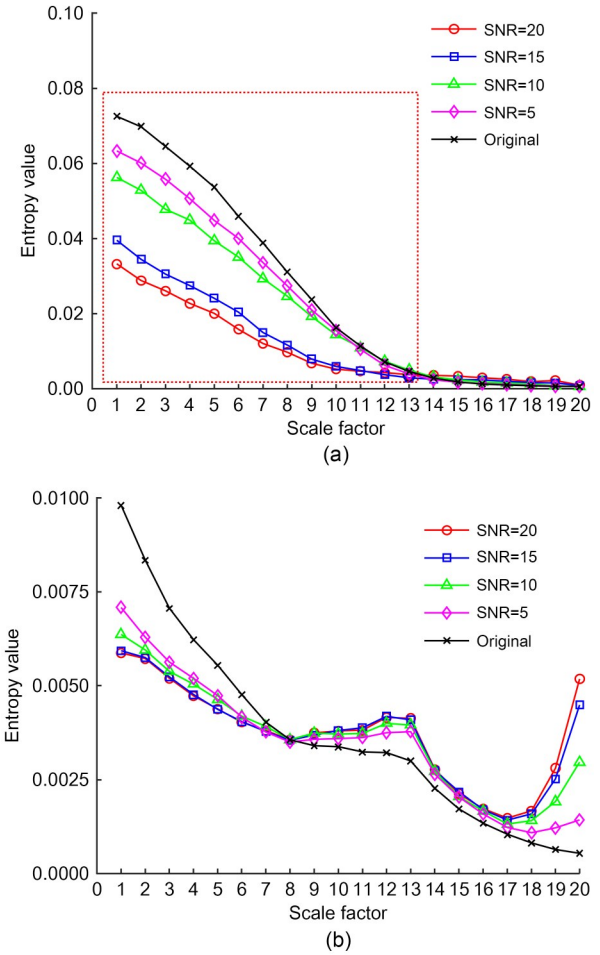


Fig. 10 Entropy value results for APVS under different SNR levels: (a) CIR; (b) CMRWPE

scales 9 and 13, the CIR curves progressively approximate the original signal. When the scales exceed 14, the curves for different SNR levels converge. This indicates that beyond a specific scale threshold, CIR enables stable feature extraction and exhibits robust anti-noise performance.

To evaluate the anti-noise robustness of the proposed method CIR and the competing approach, CMRWPE for weak fault diagnosis, their diagnostic accuracies obtained via the SVM classifier are compared across SNR levels ranging from 0 to 20 dB.

As shown in Fig. 11, CMRWPE exhibits superior performance under low SNR levels (0–10 dB), maintaining a stable accuracy above 60.0% and peaking at 73.5%, which highlights its strong robustness against heavy background noise. In contrast, the CIR starts at a lower accuracy of 43.0% at 0 dB but shows a steady improvement with increasing SNR, eventually

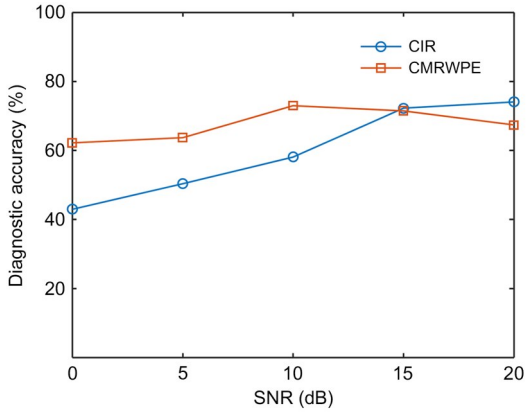


Fig. 11 Diagnostic accuracy comparison at different SNR levels

surpassing the CMRWPE at 15 dB and reaching 74.5% at 20 dB. The core finding is that CMRWPE is more suitable for strong-noise environments, while CIR demonstrates better performance as the signal quality improves.

4.3 Ablation experiment

Ablation experiments quantitatively assess the efficacy of each module in the CIR-PS model (A9) for APVS diagnosis. We use the traditional model (A10) as the reference. It applies variational mode decomposition (VMD) to process raw signals, leverages PE to capture fault features, and finally uses SVM to complete fault identification. Within this framework, ablation models are constructed by progressively replacing individual modules of the A9 model with their counterparts from the A10 model, as detailed in Table 4. The symbol '√' denotes the adoption of the baseline A9 model method for the corresponding module.

In ablation experiments, the F_1-score (Naidu et al., 2023) is employed as an evaluation metric to assess model reliability. This indicator represents the harmonic mean of precision and recall, defined as follows:

$$\begin{cases} F_1=\dfrac{2P_rR_e}{P_r+R_e}, \\ P_r=\dfrac{N_{TP}}{N_{TP}+N_{FP}}, \\ R_e=\dfrac{N_{TP}}{N_{TP}+N_{FN}}, \end{cases} \tag{9}$$

where P_r and R_e denote the precision and recall, respectively; N_{TP} denotes the correctly identified faulty samples; N_{FP} denotes the misdiagnosed normal samples; N_{FN} denotes the missed faulty samples.

Fig. 12 demonstrates the importance of each module in the proposed method for weak fault diagnosis. Removing any key module leads to a significant drop in the F_1-score, exceeding 0.40 in some cases. The dual-module ablation further reveals synergistic and compensatory effects between modules, with some components showing strong dependencies on others. Overall, the results confirm that the collaborative optimization of all modules is critical to maintaining stable performance and high diagnostic accuracy.

Table 4 Experimental settings for each generalization task in the ablation experiment

Model	Module			
	Signal decomposition	Feature selection	Feature extraction	ML
A1		√	√	√
A2	√		√	√
A3	√	√		√
A4	√	√	√	
A5			√	√
A6		√	√	
A7	√			√
A8		√		√
A9	√	√	√	√
A10				

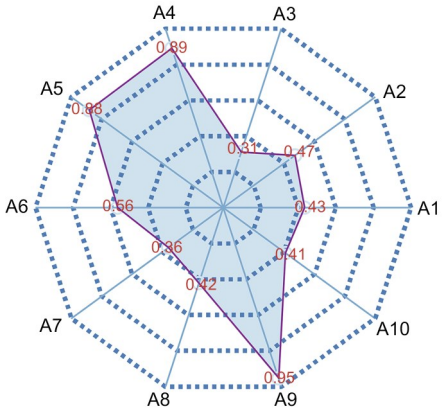


Fig. 12 Fault diagnosis results in terms of F_1-score

4.4 Machine learning analysis

To validate the impact of ML on CIR performance, back propagation (BP), SVM, extreme learning machine

(ELM), partial least squares (PLS), PSO-BP, and PSO-SVM were selected for comparison. BP exhibits strong fitting capability, SVM demonstrates superior generalization and noise robustness, PLS adapts well to high-dimensional features, ELM offers rapid training speed, and methods based on PSO enhance performance through parameter adjustment.

The confusion matrices of six ML models are presented in Fig. 13, showing their performance on the APVS fault classification task. The SVM achieves the lowest accuracy of 68.3%, while both PSO-BP and PSO-SVM exceed 93.0%, confirming that PSO-SVM is highly effective for subtle fault identification.

To comprehensively evaluate the effectiveness of the proposed method, six ML models are compared across accuracy, F_1-score, and recall metrics, as shown in Fig. 14.

As shown in the bar chart in Fig. 14, this illustrates a comparison of the performance of six ML models across three key metrics. The results show that PSO-SVM achieves the highest and most balanced performance across all three metrics, outperforming other models and demonstrating its effectiveness in reducing both misdiagnosis and missed diagnosis.

4.5 Comparison of acoustic and vibration signals

The generalization capability of the CIR-PS model was validated based on IEPE and MEMS vibration signals. Calculate the parameter $\boldsymbol{T}_{k,t}$ separately for each individual vibration signal and determine t=4 and t=3 for the MEMS and IEPE signals, respectively. The box plot shows the distributions of different metrics for MEMS and IEPE signals, aiming to determine the optimal performance indicator, as shown in Fig. 15.

From the results presented in Fig. 15, the high-frequency components of the IEPE vibration signal are concentrated in the range of 1–4; thus, the upper limit is set to 4. MEMS vibration signal shows high-frequency components covering 1–3, and the corresponding upper limit is determined as 3. Features are extracted from the screened IMFs, and the obtained feature set is input into the PSO-SVM for fault classification and identification. The ML classification results are presented in Figs. 16–18. These visualizations

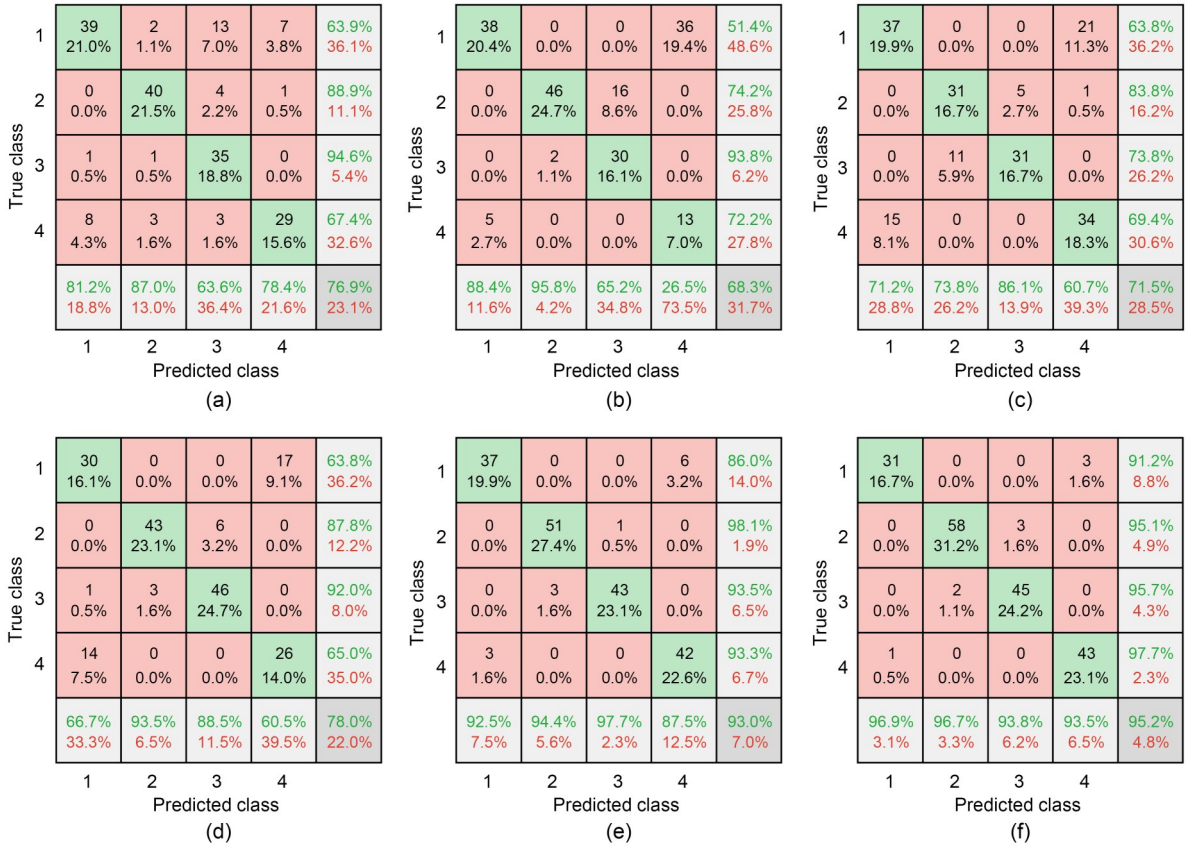


Fig. 13 Confusion matrices of six ML models: (a) BP; (b) SVM; (c) ELM; (d) PLS; (e) PSO-BP; (f) PSO-SVM

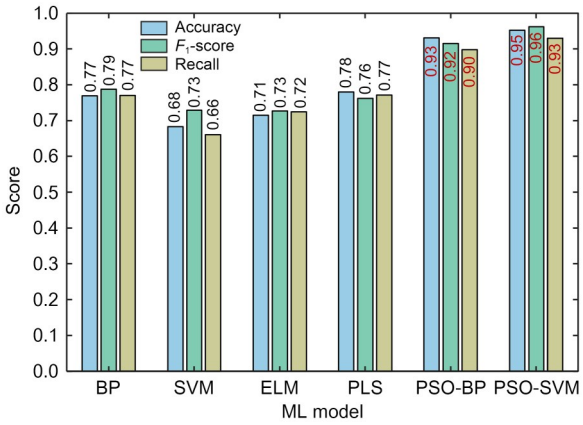


Fig. 14 Performance comparison chart of six ML models

quantify label consistency and class-wise classification performance, while revealing fault identification accuracy and misclassification patterns.

The results indicate that the CIR-PS delivers high recognition accuracy in APVS while maintaining favorable precision in the diagnosis of MEMS and IEPE signals. The diagnostic accuracy for all three signal types exceeded 95.2%, with vibration signal accuracy reaching no less than 96.4%, confirming that CIR-PS possesses generalizability across different signal types.

5 Conclusions

This study focuses on the accurate and efficient diagnosis of subtle bearing weak faults in EDS. Based on acoustic and vibration signal data acquired from a laboratory EDS test bench, the overall research conclusions are as follows:

(1) A novel feature selection method, namely, the IE-MSFS method, is proposed to tackle the issues of noise interference and redundancy in weak fault diagnosis. It employs multi-indicator screening of IMF components to suppress redundant features and enhance the representation of weak fault features under noisy conditions.

(2) Based on the proposed IE-MSFS method, the CIR-PS model is validated using three typical EDS weak fault acoustic signals. Experimental results under

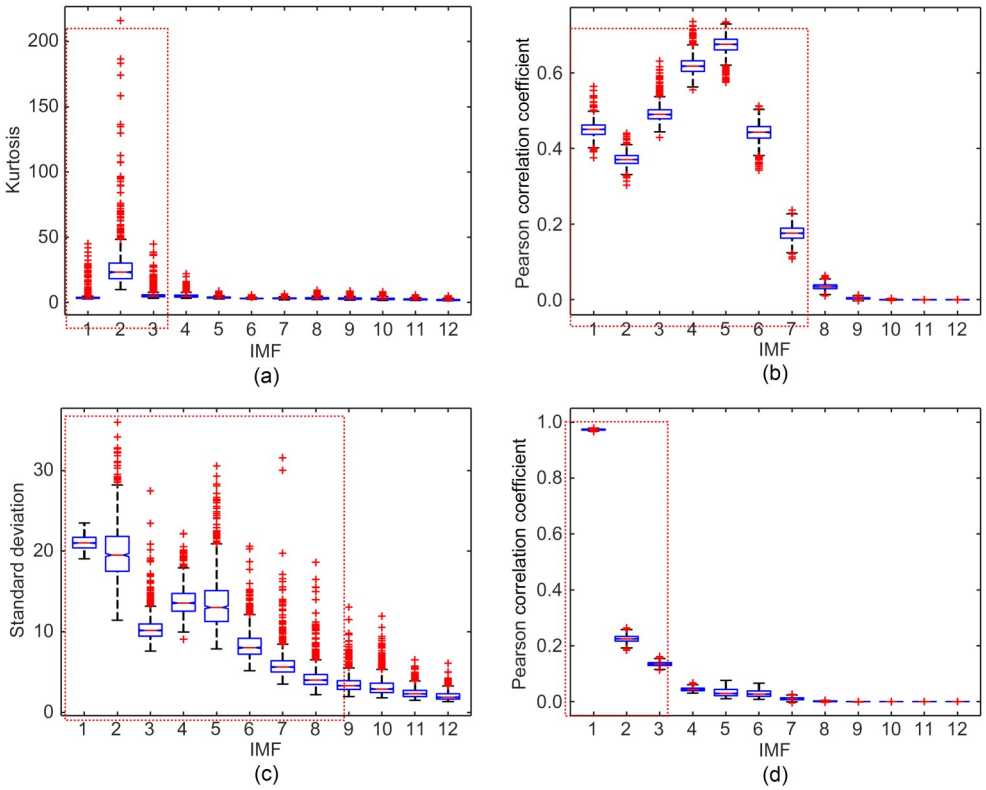


Fig. 15 Box diagrams of different matrices for MEMS and IEPE signals: (a) kurtosis for the MEMS signal; (b) Pearson correlation coefficient for the MEMS signal; (c) standard deviation for the IEPE signal; (d) Pearson correlation coefficient for the IEPE signal

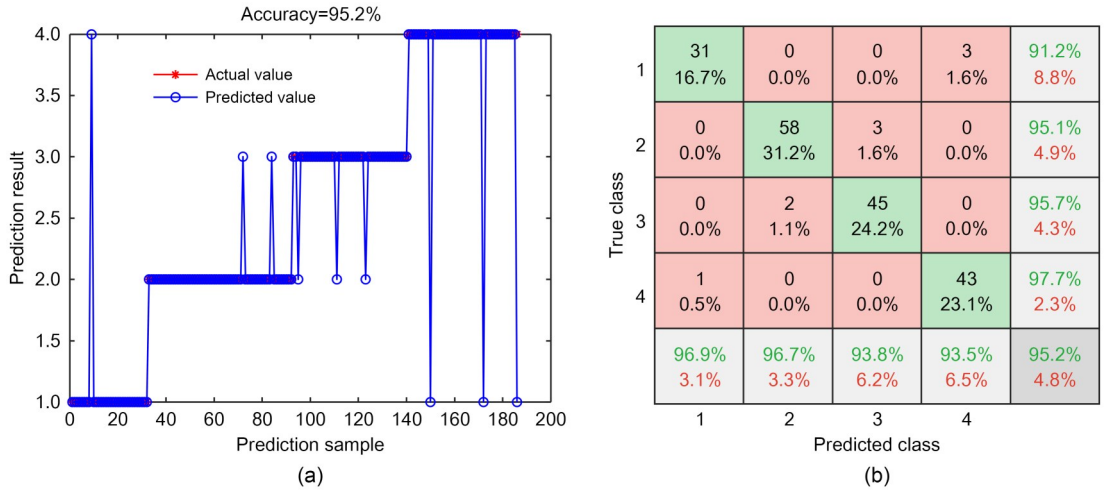


Fig. 16 ML of the APVS: (a) comparison of test set prediction results; (b) confusion matrix of test data

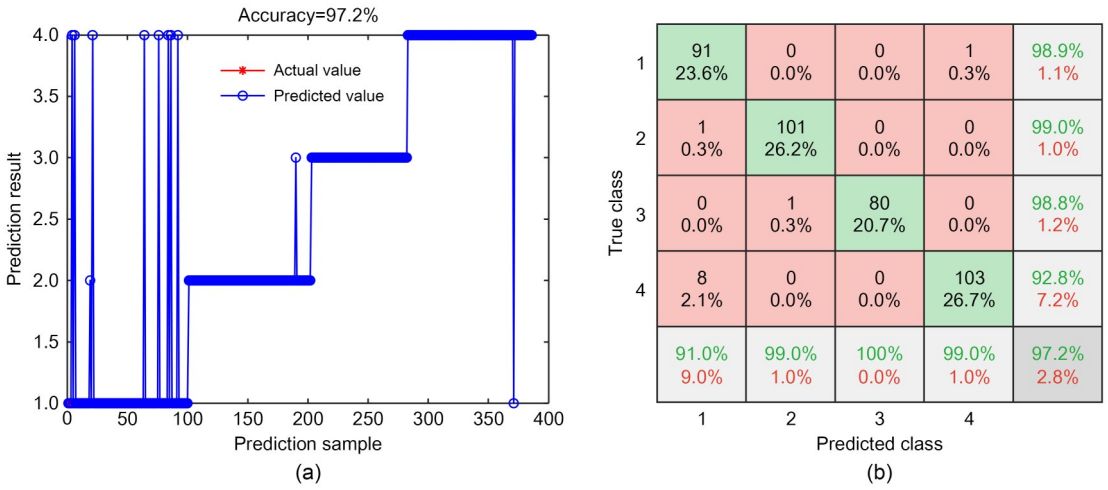


Fig. 17 ML of high-quality vibration signals: (a) comparison of test set prediction results; (b) confusion matrix of test data

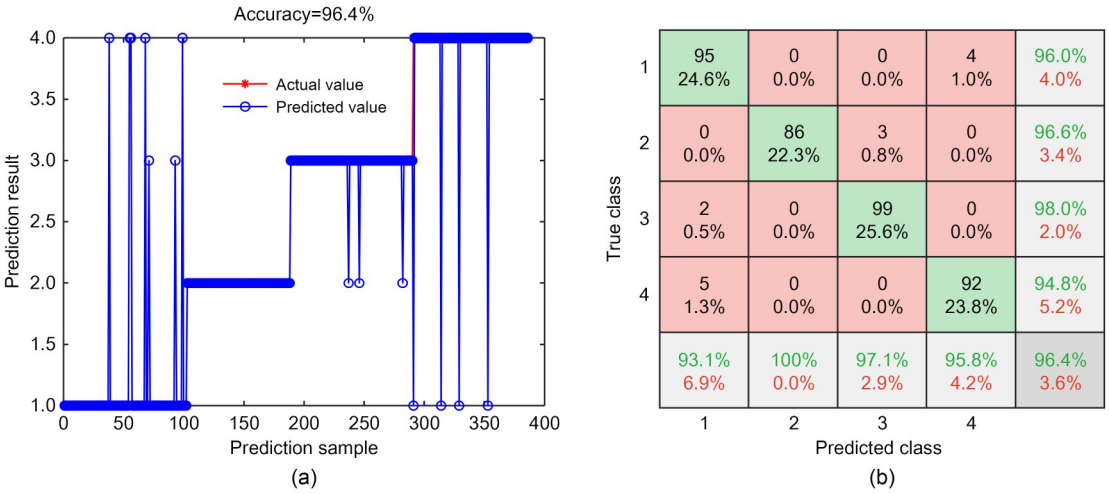


Fig. 18 ML of low-quality vibration signals: (a) comparison of test set prediction results; (b) confusion matrix of test data

different SNR levels confirm its excellent anti-noise robustness, with a diagnostic accuracy higher than 95.2%.

(3) Validations on two vibration signal datasets show that the CIR-PS model can effectively distinguish ORF and IRF. It achieves a minimum accuracy of 96.4%, demonstrating good generalization and practicability.

The present study identifies acoustic signals for subtle bearing faults in EDS to facilitate noncontact diagnosis. Although utilizing acoustic and vibration data is effective for single weak faults under stable laboratory conditions, it fails to address compound faults or time-varying operating conditions. Future research will focus on the detection and validation of compound weak faults under variable conditions to support practical engineering applications.

Acknowledgments

This work is supported by the Young Scientists Fund of the National Natural Science Foundation of China (No. 52301328). The authors would like to express their gratitude to NIO Inc., China for fruitful discussions on topics relevant to this work.

Author contributions

Cong YUE and Jingwen KANG designed the research and revised and edited the final version. Jingwen KANG and Yonghao ZHAO processed the corresponding data. Jingwen KANG wrote the first draft of the manuscript. Cong YUE and Ping CHENG helped to organize the manuscript.

Conflict of interest

Cong YUE, Jingwen KANG, Yonghao ZHAO, and Ping CHENG declare that they have no competing financial interests or personal relationships that could have appeared to influence the work reported in preparing this article.

Declaration on the use of generative AI tools

No generative AI tools were used in the preparation of this manuscript.

Data availability

The data that support the findings of this study are available from the corresponding author upon reasonable request.

References

Chen BY, Song DL, Zhang WH, et al., 2021. A performance enhanced time-varying morphological filtering method for bearing fault diagnosis. *Measurement*, 176:109163. https://doi.org/10.1016/j.measurement.2021.109163

Chen WG, Li JN, Wang Q, et al., 2021. Fault feature extraction and diagnosis of rolling bearings based on wavelet thresholding denoising with CEEMDAN energy entropy and PSO-LSSVM. *Measurement*, 172:108901. https://doi.org/10.1016/j.measurement.2020.108901

Gao HL, Wu CL, Zhu DD, et al., 2023. Feature extraction method of underwater acoustic signals using VMD and reverse weighted permutation entropy. 2023 6th International Conference on Information Communication and Signal Processing (ICICSP), p.465-470. https://doi.org/10.1109/ICICSP59554.2023.10390552

Gong HH, Li YY, Zhang JN, et al., 2024. A new filter feature selection algorithm for classification task by ensembling Pearson correlation coefficient and mutual information. *Engineering Applications of Artificial Intelligence*, 131: 107865. https://doi.org/10.1016/j.engappai.2024.107865

Hou YC, Zhou CQ, Tian CM, et al., 2022. Acoustic feature enhancement in rolling bearing fault diagnosis using sparsity-oriented multipoint optimal minimum entropy deconvolution adjusted method. *Applied Acoustics*, 201: 109105. https://doi.org/10.1016/j.apacoust.2022.109105

Husain I, Ozpineci B, Islam MS, et al., 2021. Electric drive technology trends, challenges, and opportunities for future electric vehicles. *Proceedings of the IEEE*, 109(6):1039-1059. https://doi.org/10.1109/JPROC.2020.3046112

Jusup M, Holme P, Kanazawa K, et al., 2022. Social physics. *Physics Reports*, 948:1-148. https://doi.org/10.1016/j.physrep.2021.10.005

Kuntoğlu M, Salur E, Gupta MK, et al., 2021. A state-of-the-art review on sensors and signal processing systems in mechanical machining processes. *The International Journal of Advanced Manufacturing Technology*, 116(9-10):2711-2735. https://doi.org/10.1007/s00170-021-07425-4

Lao ZP, He DQ, Wei ZX, et al., 2023. Intelligent fault diagnosis for rail transit switch machine based on adaptive feature selection and improved LightGBM. *Engineering Failure Analysis*, 148:107219. https://doi.org/10.1016/j.engfailanal.2023.107219

Liu Y, Xu ZF, He YL, et al., 2025. Acoustic fault diagnosis method for rotating machinery based on improved spectral subtraction and CNN-TCN model. *Measurement*, 256: 118482. https://doi.org/10.1016/j.measurement.2025.118482

Long JC, Wang XP, Zhou W, et al., 2021. A comprehensive review of signal processing and machine learning technologies for UHF PD detection and diagnosis (I): preprocessing and localization approaches. *IEEE Access*, 9: 69876-69904. https://doi.org/10.1109/ACCESS.2021.3077483

Lu N, Li ZL, Liu D, et al., 2025. A feature extraction method for rotating machinery fault diagnosis based on a multiscale entropy fusion strategy and GA-RL-LDA model. *Soft Computing*, 29(3):1747-1765. https://doi.org/10.1007/s00500-025-10484-4

Manivannan R, Samidurai R, Cao JD, et al., 2020. Design of

resilient reliable dissipativity control for systems with actuator faults and probabilistic time-delay signals via sampled-data approach. *IEEE Transactions on Systems, Man, and Cybernetics: Systems*, 50(11):4243-4255. https://doi.org/10.1109/TSMC.2018.2846645

Meng DB, Wang HT, Yang SY, et al., 2022. Fault analysis of wind power rolling bearing based on EMD feature extraction. *Computer Modeling in Engineering & Sciences*, 130(1):543-558. https://doi.org/10.32604/cmes.2022.018123

Miao YH, Zhang BY, Li CH, et al., 2023. Feature mode decomposition: new decomposition theory for rotating machinery fault diagnosis. *IEEE Transactions on Industrial Electronics*, 70(2):1949-1960. https://doi.org/10.1109/TIE.2022.3156156

Naidu G, Zuva T, Sibanda EM, 2023. A review of evaluation metrics in machine learning algorithms. *In*: Silhavy R, Silhavy P (Eds.), Artificial Intelligence Application in Networks and Systems. Springer, Cham, Switzerland, p.15-25. https://doi.org/10.1007/978-3-031-35314-7_2

Nawfal Mustafa M, 2021. Classification of maintenance techniques and diagnosing failures methods. *Journal of Physics: Conference Series*, 2060(1):012014. https://doi.org/10.1088/1742-6596/2060/1/012014

Odhiambo Omuya E, Onyango Okeyo G, Waema Kimwele M, 2021. Feature selection for classification using principal component analysis and information gain. *Expert Systems with Applications*, 174:114765. https://doi.org/10.1016/j.eswa.2021.114765

Raj KK, Kumar S, Kumar RR, 2025. Systematic review of bearing component failure: strategies for diagnosis and prognosis in rotating machinery. *Arabian Journal for Science and Engineering*, 50(8):5353-5375. https://doi.org/10.1007/s13369-024-09866-x

Tang YH, Zhang CY, Wu JZ, et al., 2024. Deep learning-based bearing fault diagnosis using a trusted multiscale quadratic attention-embedded convolutional neural network. *IEEE Transactions on Instrumentation and Measurement*, 73:3513215. https://doi.org/10.1109/TIM.2024.3374311

Wan LJ, Gong K, Zhang G, et al., 2021. An efficient rolling bearing fault diagnosis method based on spark and improved random forest algorithm. *IEEE Access*, 9:37866-37882. https://doi.org/10.1109/ACCESS.2021.3063929

Wang B, Qiu WT, Hu X, et al., 2024. A rolling bearing fault diagnosis technique based on recurrence quantification analysis and Bayesian optimization SVM. *Applied Soft Computing*, 156:111506. https://doi.org/10.1016/j.asoc.2024.111506

Wang XL, Zheng JD, Ni Q, et al., 2022. Traversal index enhanced-gram (TIEgram): a novel optimal demodulation frequency band selection method for rolling bearing fault diagnosis under non-stationary operating conditions. *Mechanical Systems and Signal Processing*, 172:109017. https://doi.org/10.1016/j.ymssp.2022.109017

Wang ZR, Huang HA, Wang YR, 2021. Fault diagnosis of planetary gearbox using multi-criteria feature selection and heterogeneous ensemble learning classification. *Measurement*, 173:108654. https://doi.org/10.1016/j.measurement.2020.108654

Yang DP, Wang XL, Wang YS, et al., 2019. A multi-source fusion algorithm for high-accuracy signal reconstruction of vehicle interior noise on passenger ear-sides. *Applied Acoustics*, 148:75-85. https://doi.org/10.1016/j.apacoust.2018.12.017

Yao JM, Liang W, Duan LX, et al., 2025. Non-contact intelligent diagnosis method for key components in energy equipment based on acoustic signal and deep learning. *Applied Energy*, 398:126380. https://doi.org/10.1016/j.apenergy.2025.126380

Yue C, Zhu Y, Cheng P, et al., 2024. A novel method for identifying resonance frequency band in weak bearing fault diagnosis of electric driving system. *Shock and Vibration*, 2024:2804173. https://doi.org/10.1155/2024/2804173

Yue C, Dong JB, Zhu Y, et al., 2025. A novel fault diagnosis model for rolling bearings in electric drive systems using multi-scale improved weighted permutation entropy and radial basis function neural network. *Insight-Non-Destructive Testing and Condition Monitoring*, 67(1):39-46. https://doi.org/10.1784/insi.2025.67.1.39

Zhang XL, Han P, Xu L, et al., 2020. Research on bearing fault diagnosis of wind turbine gearbox based on 1DCNN-PSO-SVM. *IEEE Access*, 8:192248-192258. https://doi.org/10.1109/ACCESS.2020.3032719

Zhao JD, Wang WM, Huang J, et al., 2025. A comprehensive review of deep learning-based fault diagnosis approaches for rolling bearings: advancements and challenges. *AIP Advances*, 15(2):020702. https://doi.org/10.1063/5.0255451